



## Oxidation in ceria infiltrated metal supported SOFCs – A TEM investigation

Ruth Knibbe\*, Hsiang-Jen Wang<sup>1</sup>, Peter Blennow, Karl Thydén, Åsa H. Persson, Lars Mikkelsen, Trine Klemensø

Department of Energy Conversion and Storage, Technical University of Denmark, PO Box 49, DK-4000 Roskilde, Denmark

### HIGHLIGHTS

- Ceria infiltration of metal supported SOFC anode improves OCV oxidation resistance.
- During processing the ceria converts to CeFeO<sub>3</sub> which protects the metal backbone.
- The ohmic resistance of the infiltrated SOFC increases during long-term tests.
- Ohmic resistance increase is due to anode active site oxidation.
- Analytical TEM is used to gain understanding of the complex anode structure.

### ARTICLE INFO

#### Article history:

Received 10 September 2012

Received in revised form

15 November 2012

Accepted 16 November 2012

Available online 28 November 2012

#### Keywords:

Analytical transmission electron microscopy

Metal supported solid oxide fuel cells

Fuel cell durability

CeFeO<sub>3</sub>

Ceria

### ABSTRACT

The oxidation resistance of the Fe–Cr alloy backbone structure of metal supported solid oxide fuel cells is significantly improved when infiltrated with gadolinium doped ceria (CGO) particles. The mechanism for the improved oxidation behaviour is elucidated using various analytical transmission electron microscopy (TEM) techniques including energy-dispersive X-ray spectroscopy and electron energy-loss spectroscopy of focus ion beamed TEM samples. The infiltrated CGO is predominately converted into CeFeO<sub>3</sub> after high temperature processing, protecting the alloy. A thin layer of Cr-oxide is observed to be sandwiched between the CeFeO<sub>3</sub>/CGO layers and the Fe–Cr alloy particles. Despite the improved oxidation resistance at open circuit voltage, during fuel cell testing accelerated oxidation is observed at the triple phase boundaries.

© 2012 Elsevier B.V. All rights reserved.

## 1. Introduction

Solid oxide fuel cells (SOFC) are high temperature electrochemical devices, which convert chemical energy, bound in a fuel, directly into electrical energy and heat. Due to the versatility of the SOFC technology, and the high efficiencies which can be reached, this technology is attractive for energy conversion systems in both stationary and mobile applications [1–4].

Metal supported SOFC stack technologies are believed to offer an alternative to conventional electrode- and electrolyte-supported SOFCs. Metallic substrates are advantageous as they are both good thermal conductors and ductile. This may improve thermal shock resistance, and lower the internal temperature gradients, allowing

quicker start-up [5]. If successful, metal-based SOFC stack technologies have the potential to improve functionality, reliability, reproducibility and affordability of the SOFC stack [6].

Despite these potential advantages, the cell fabrication process is one major challenge holding back metal supported SOFCs development [6]. Most metal supported cell (MSC) developers started out using conventional yttria stabilised zirconia and nickel cermet anodes – typically used in ceramic anode-supported cells. However, to protect the metal support from oxidation, low pO<sub>2</sub> atmosphere is required during elevated temperature sintering causing strong Ni coarsening and agglomeration. This reduces both the triple phase boundary length and the Ni-particle connectivity – reducing the anode performance. Furthermore, during sintering or high temperature operation, interdiffusion will occur between Ni-based anodes in direct contact with Fe–Cr based metal supports. Interdiffusion can form Ni–Cr–Fe alloys or insulating oxides in the anode layer, or result in reduced oxidation resistance and increased thermal expansion coefficient in the support, all which are detrimental to cell performance and stability [6,7].

\* Corresponding author. Present address: Industrial Research Limited, PO Box 31310, Wellington 5040, New Zealand. Tel.: +64 4 931 3092; fax: +64 4 566 6004.

E-mail addresses: [rknibbe@hotmail.com](mailto:rknibbe@hotmail.com), [r.knibbe@irl.cri.nz](mailto:r.knibbe@irl.cri.nz) (R. Knibbe).

<sup>1</sup> Present address: Department of Materials Science and Engineering, Case Western Reserve University, Cleveland 44106-7204, USA.

The Technical University of Denmark has developed an unconventional half cell design where these problems can be circumvented by using an alternative anode structure. The cell design is based on porous, electronically conductive layers into which electro-catalytically active anode materials (gadolinium doped ceria (CGO) and minor amounts of Ni) are infiltrated after sintering. The multilayered structure is obtained by conventional low-cost ceramic processing techniques such as tape casting and screen printing [8]. Despite the encouraging electrochemical performance and durability, there is still a need for improved long-term durability [8–10]. The novel anode design contains stainless steel particles where an oxide scale (corrosion layer) forms during long-term testing. This corrosion layer is believed to be one of the causes for the degradation observed during MSC galvanostatic testing [9]. In order to improve the durability and robustness of the MSC there is a need to further understand the oxide scale formation during fuel cell operation.

This paper includes a detailed microanalysis study of the infiltrated fuel electrode after electrochemical testing. Various analytical transmission electron microscopy (TEM) techniques, such as energy-dispersive X-ray spectroscopy (EDS) and electron energy-loss spectroscopy (EELS), have been used to investigate the effect of the infiltrated electrocatalysts on the performance, durability, and oxide scale formation of MSCs.

## 2. Experimental

### 2.1. Sample fabrication

The half cell (Fe–Cr alloy support/anode/electrolyte) was co-sintered under proprietary conditions above 1100 °C in a low oxygen partial pressure ( $p_{O_2}$ ) atmosphere (H<sub>2</sub>–Ar). The Fe–Cr alloy support is a porous Fe–Cr–Mn (Fe as base element, 22% Cr, 0.4% Mn) alloy (referred to alloy in the text), the anode is a cermet with the aforementioned alloy and 3 mol% Y<sub>2</sub>O<sub>3</sub>-stabilised ZrO<sub>2</sub> (YSZ) and the electrolyte is composed of ZrO<sub>2</sub> co-doped with Sc<sub>2</sub>O<sub>3</sub> and Y<sub>2</sub>O<sub>3</sub> (ScYSZ). After sintering, the porous alloy support and anode were infiltrated with the electro-catalytic active, nano-sized Ce<sub>0.8</sub>Gd<sub>0.2</sub>O<sub>1.9</sub> (CGO) and Ni particles. More details about the fabrication process are described elsewhere [8,11]. The infiltrated oxide phases amounted to approximately 3 wt% of the half cell.

The cathode and a cathode contact layer were applied onto the electrolyte of the half cell by screen printing. The cathode layer was a La<sub>0.58</sub>Sr<sub>0.4</sub>Co<sub>0.2</sub>Fe<sub>0.8</sub>O<sub>3-δ</sub>/Ce<sub>0.9</sub>Gd<sub>0.1</sub>O<sub>2-δ</sub> composite, and the contact layer (La<sub>0.6</sub>Sr<sub>0.4</sub>)<sub>0.99</sub>CoO<sub>3-δ</sub>. The screen-printed layers were fired in-situ during the initial phase of the cell testing at 750 °C for 10 h.

### 2.2. Electrochemical characterisation

The footprint size of the tested cell was 5 × 5 cm<sup>2</sup> and the active area 16 cm<sup>2</sup>, which was defined by the area of the screen-printed cathode. The cell was tested in an alumina housing used for conventional anode-supported cells, and the test house and positions of voltage probes and current pick-up points were as described in [4]. The Pt voltage and current probes were contacted to the current collector plates which were mounted into the test housing. A Ni plate was used as a current collector plate on the anode side, and a Pt plate on the cathode side.

Corrugated metal meshes were used as contact components between the cell and the current collector plates in the alumina housing. This way, the contact components also act as gas distribution layers. On the anode side, a corrugated Ni felt was used as contact component, and partly corrugated Pt meshes were used as cathode contact components.

The MSC was galvanostatically durability tested for 170 h at current density of 0.25 A cm<sup>-2</sup>, 650 °C, with low fuel and oxygen utilisation (both below 10%), and with H<sub>2</sub>-3% H<sub>2</sub>O as fuel, and air as oxidant gas. The MSC was characterised before and after SOFC operation by polarisation curves and electrochemical impedance spectroscopy (EIS) measurements with characterisation conditions of 650 °C, with H<sub>2</sub> fuel containing either 3% water or 20% water supplied to the anode, and air or oxygen supplied to the cathode. A Solartron 1260 or Solartron 1255B frequency response analyser was used for the EIS measurements, which carried out with a 85 mA amplitude (60 mA rms) in the 0.08 Hz–82.5 kHz frequency range.

### 2.3. Corrosion testing

Half cells with and without CGO-Ni infiltration were fabricated and tested for long-term corrosion stability. The corrosion test was conducted at 650 °C in simulated outlet anode gas, an Ar–H<sub>2</sub>–H<sub>2</sub>O atmosphere with pH<sub>2</sub>O/pH<sub>2</sub> = 9 (simulating the pO<sub>2</sub> at the fuel outlet when having 90% fuel utilization). After 2000 h corrosion testing the half cell microstructures were studied.

### 2.4. Electron microscopy

The MSC and the half cell samples used for scanning electron microscopy (SEM) analysis were vacuum embedded in epoxy resin; ground using SiC paper; polished using 6, 3 and 1 μm diamond paste, and then carbon coated to eliminate the surface charging. The samples were observed using a Zeiss Crossbeam 1540XB equipped with a field emission gun (FEG). To accentuate average atomic number differences, the SEM was operated in backscattered electron mode at 10 or 15 keV.

A TEM sample was prepared using the focused ion beam (FIB) on the aforementioned Zeiss SEM. The FIB was operated at 30 keV during milling. All TEM work was done on a JOEL 3000F, a field-emission analytical 300 kV TEM equipped with a Gatan Imaging Filter (GIF) and a scanning TEM (STEM) unit. An Oxford Instruments INCA system was used for chemical analysis, including both line scan EDS and elemental mapping utilizing 1 nm probe size. All concentration profiles were plotted using cation percentage by excluding the O content. EELS spectra were collected using a Gatan EELS detector at 297 keV with a dispersion of 0.2 or 0.5 eV/pixel. All EELS data presented are background-subtracted and plural scattering removed. The same background-subtracted window was applied to all spectra acquired from both point EELS spectra and STEM-EELS spectra.

## 3. Results

### 3.1. Electrochemical characterisation

**Fig. 1** shows polarisation and power curves recorded before and after galvanostatic durability testing of the MSC at 650 °C, supplied with H<sub>2</sub>-3% H<sub>2</sub>O (24 L h<sup>-1</sup>) to the anode and air to the cathode (140 L h<sup>-1</sup>). The area specific resistances (ASR) were calculated from the secant at 0.7 V, yielding an ASR of 0.86 and 1.43 Ω cm<sup>2</sup> before and after durability testing, respectively.

The EIS data acquired under current during testing is presented in Nyquist plots in **Fig. 2(c)**. The major change in the EIS curves is due to an increased ohmic resistance ( $R_s$ ) causing the EIS curves to shift to the right during MSC durability testing. In contrast, the polarisation resistance ( $R_p$ ) remains relatively constant. The  $R_s$  and  $R_p$  values obtained for **Fig. 2(a)** are the highest and lowest real impedance values on the Nyquist plots (**Fig. 2(c)**). In the Nyquist plots the high frequency end (left hand side) is beginning to show an additional high frequency arc. This is attributed to reaction layer

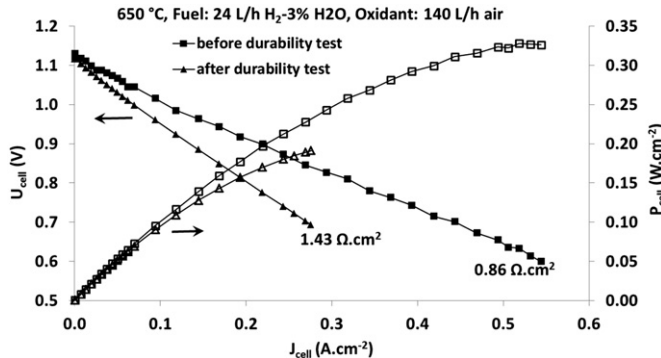


Fig. 1. Polarisation and power curves recorded before and after MSC durability testing.

at the cathode–electrolyte interface in this particular system [9]. Although it would be best to model the data, to obtain the  $R_s$  and  $R_p$  values, considerable extrapolation is required to fit the high frequency end of the impedance data.

The  $R_s$  rise is concomitant with an increased anode in-plane voltage (see Fig. 2(a)), suggesting that the Fe–Cr alloy matrix causes the ASR increase possibly through oxidation. From EIS collected at open circuit voltage (OCV) before and after durability testing (Fig. 2(b)), it is observed that the small  $R_p$  change is characterised by an increased impedance at very high frequencies (>10 kHz), and to some degree at intermediate frequencies around 500 Hz. At the start of durability testing ( $0.25 \text{ A cm}^{-2}$ ) the overvoltage (cell polarisation) across the cell was ca. 330 mV, of which 57% was due to  $R_s$  and the remaining 43% to  $R_p$ . During testing the  $R_s$  increased by 17% and the  $R_p$  by 5%.

The theoretical OCV (calculated from the Nernst equation) for the MSC supplied with  $\text{H}_2\text{-}3\% \text{ H}_2\text{O}$  ( $24 \text{ L h}^{-1}$ ) to the anode and air to

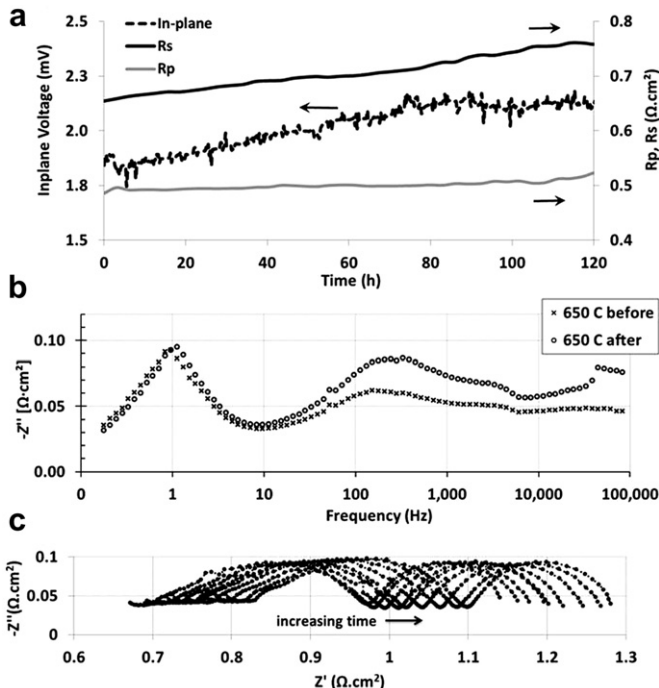


Fig. 2. (a)  $R_p$ ,  $R_s$  and in-plane voltage degradation during MSC durability testing. (b) Bode representation of the imaginary part of EIS data recorded before and after MSC durability testing. The EIS data were recorded at OCV, 650 °C, and with  $\text{H}_2\text{-}20\% \text{ H}_2\text{O}$  as fuel, and air as oxidant. (c) Nyquist plots of the EIS data acquired, under current, during MSC durability testing.

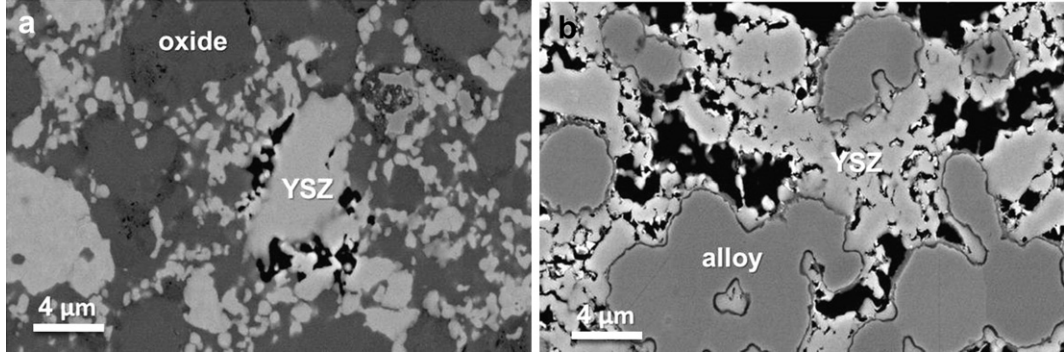
the cathode ( $140 \text{ L h}^{-1}$ ) is 1129 mV. The measured OCV before durability testing was exactly 1129 mV, however, after durability testing it was 12 mV lower at 1117 mV. The small OCV difference could be caused by either electronic (short-circuiting) or gas leaks (i.e. gas permeation between the fuel and oxidant gas compartments through electrolyte cracks or externally through the seals). The set-up gas tightness was evaluated before durability testing, based on equivalent leak currents as described elsewhere [9]. Before durability testing, low leak currents were measured (below  $12 \text{ mA cm}^{-2}$ ) which were relatively flow independent, indicating no major flaws in the seals or electrolyte. The small drop in OCV measured after the durability testing (12 mV) could be an indication of minor flaws such as micro-cracks in the seals or electrolyte during the durability testing. However, no such flaws could be clearly observed after the durability testing.

### 3.2. Microstructural characterisation

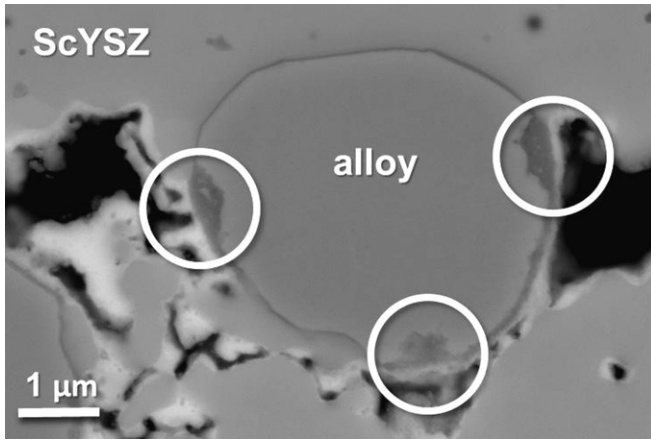
Fig. 3 are two representative micrographs of an uninfiltrated and infiltrated half cell, which have been corrosion-tested in simulated outlet gas for 2000 h. Three distinct regions can be observed in the uninfiltrated sample (Fig. 3(a)): porosity, metal oxide and YSZ which appear black, dark grey and grey respectively, due to the average atomic number differences. In comparison, four distinct regions are observed in the infiltrated sample (Fig. 3(b)): porosity, metal oxide, Fe–Cr alloy and YSZ which have a progressively lighter grey scale. It is evident that the uninfiltrated sample (Fig. 3(a)) is strongly oxidised whereas the infiltrated sample (Fig. 3(b)) are only partially oxidised with a thin oxide layer encapsulating the Fe–Cr alloy particles. In Fig. 3(b) the metal oxide region is a thin even layer (ca. 90 nm thick), covering the Fe–Cr alloy particles, irrespective of the surroundings, i.e. adjacent to a pore or under several microns of YSZ. However, once a current is drawn across the MSC (Fig. 4) the situation is altered. As with the corrosion-tested half cells, a thin oxide region (ca. 40 nm thick) is observed around the Fe–Cr alloy, but there are also regions with accelerated oxide formation (ca. 500 nm thick) in the three phase boundary (TPB) regions.

Fig. 5 is an overview high angle annular dark field scanning transmission electron microscopy (HAADF-STEM) micrograph across the anode–electrolyte interface. The micrograph reveals the porous anode structure, which is constructed of Fe–Cr alloy and YSZ particles. Several regions exhibit a bright contrast in the HAADF-STEM image, e.g. areas in the Fe–Cr alloy particles and a ca. 200 nm layer on both the Fe–Cr alloy and YSZ particle surfaces (indicated by arrows). The layer contiguous to the Fe–Cr alloy is the corrosion layer, which forms during durability testing. In addition to the corrosion layers, the infiltrated CGO-Ni is observed on the external surface of the corrosion layers and also adjacent to the YSZ or ScYSZ grains. In the following section, two regions will be focused on – the layers on the Fe–Cr alloy and YSZ grains.

The distribution of elements and size of infiltrate particles around the YSZ grains is highlighted in Fig. 6, which is a phase map constructed by overlapping individual Zr, Ni, Cr, Fe and Ce elemental maps. A ca. 2–300 nm thick Ce-rich layer (light blue) coats the YSZ (red) particles and the electrolyte. In addition, Ni particles (yellow) are dispersed within the CGO layer, with larger Ni particles at the extremities of this region. More detailed elemental analysis is provided by an EDS line scan across the CGO coating on the ScYSZ electrolyte surface. Fig. 7 contains (a) a phase map, (b) a bright-field STEM (BF-STEM) image illustrating the line scan position, and (c) the corresponding concentration profile. The layer adjacent to the ScYSZ electrolyte can be characterised by 3 regions – a CGO region adjacent to the ScYSZ electrolyte, a Fe and Ce-rich region and finally a CGO region in the outermost layer. The Fe,



**Fig. 3.** Overview micrographs of Fe–Cr alloy–YSZ cermet (a) without and (b) with CGO infiltration after 2000 h, at 650 °C, in simulated outlet anode gas (Ar/H<sub>2</sub>/H<sub>2</sub>O, pH<sub>2</sub>O/pH<sub>2</sub> = 9).



**Fig. 4.** Representative micrograph of anode–electrolyte interface region of tested MSC. The alloy is surrounded by a thin oxide layer with three phase boundary regions showing increased oxidation.

Ce-rich layer has a Ce:Fe ratio close to unity – indicating CeFeO<sub>3</sub> formation.

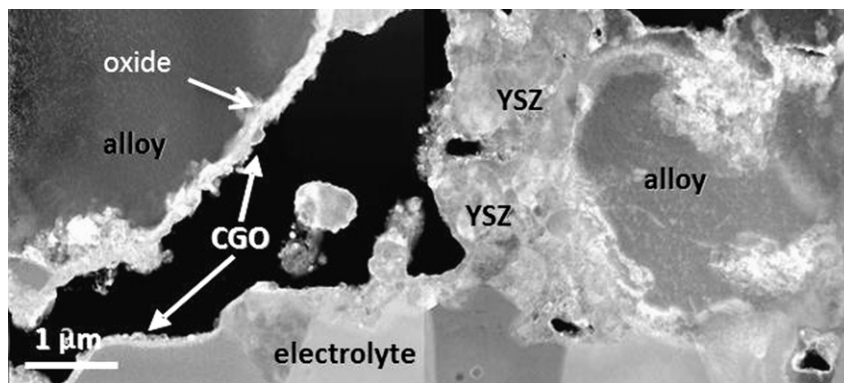
The chemical composition of the corrosion layer on the Fe–Cr alloy surface is clarified by EDS analysis presented in Fig. 8. Fig. 8 contains (a) a phase map, (b) a BF-STEM image illustrating the position of line scan, and (c) the corresponding concentration profile. In Fig. 8(a) a Cr-rich oxide layer (dark blue) surrounds the Fe–Cr alloy backbone (green). Covering the Cr-rich region is a Ce-rich (light blue) layer. Some isolated Ni particles (yellow) can be observed dispersed in this layer. Besides some very large Ni grains, the Ni particles observed in the CGO/CeFeO<sub>3</sub> region adjacent to the

Fe–Cr alloy, are more difficult to distinguish than in the CGO/CeFeO<sub>3</sub> region adjacent to the ScYSZ electrolyte (Fig. 7).

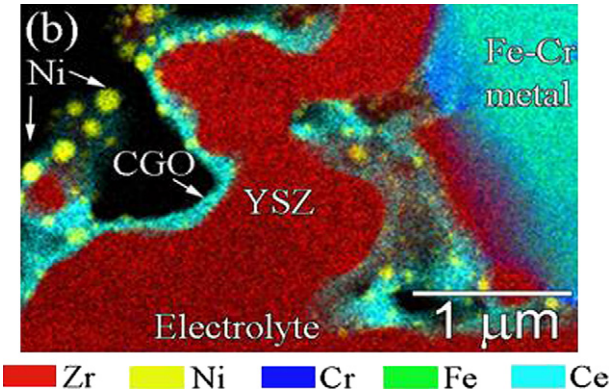
Fig. 8(c) is an EDS line scan initiating inside the Fe–Cr alloy and terminating on the outer CGO/CeFeO<sub>3</sub> surface. From the EDS line scan three regions can be distinguished – Fe–Cr alloy, corrosion layer, and CGO/CeFeO<sub>3</sub> layer. The onset of the corrosion layer is marked by an increase in the Cr concentration, coupled with a sharp Fe concentration decrease. The Cr-rich region is approximately ~60 nm thick. As Cr is the primary cation detected in this Cr-rich region, this corrosion product is considered to primarily consist of Cr-oxide. However, a small amount of Mn is also detected within this Cr-oxide region near the Fe–Cr alloy. The CGO/CeFeO<sub>3</sub> layer is characterised by a strong Ni, Fe and Ce presence – indicating Fe dissolution in CGO. As the Ce:Fe ratio is close to unity it is postulated that this is predominately CeFeO<sub>3</sub>.

Fig. 9 is a series of STEM-EELS spectra across the same interface as in Fig. 8. In the Fe–Cr alloy, only Fe and Cr edges are detected. When moving from the Fe–Cr alloy through the Cr-oxide region, the Fe peak disappears as the Cr and O edge increases – confirming a Cr-oxide region. A small Mn edge is also detected sandwiched between the Fe–Cr alloy and the Cr-oxide layer. The outermost layer is a Ce, Fe rich layer – in agreement with the EDS results.

Further confirmation of CeFeO<sub>3</sub> formation is provided by examining the Ce-M<sub>4,5</sub> edges (Fig. 10). The Ce-M<sub>4,5</sub> edge in the CGO region shows two major peaks at 883 eV (*M*<sub>5</sub>) and 910 eV (*M*<sub>4</sub>). The *M*<sub>4</sub> edge has a higher intensity in comparison to the *M*<sub>5</sub> edge with both edges flanked by a higher energy minor satellite peak (indicated with arrows) – indicative of Ce<sup>4+</sup>. The Ce-M<sub>4,5</sub> edge from the (Ce,Fe)-rich region has only two major peaks with a more intense *M*<sub>5</sub> edge than *M*<sub>4</sub> edge – indicative of Ce<sup>3+</sup>. It has been previously argued that the observation of Ce<sup>3+</sup> may be induced from beam interaction during data acquisition [12]. However, a series of



**Fig. 5.** HAADF-STEM micrograph across anode–electrolyte interface in tested MSC.



**Fig. 6.** STEM-EDS of CGO-Ni on YSZ, in anode–electrolyte interface region of tested MSC – superimposed Zr, Ni, Cr, Fe and Ce elemental maps.

spectra obtained over a period of time on a CGO area reveals no change of  $\text{Ce}^{4+}$  to  $\text{Ce}^{3+}$ . The 3+ valence state of Ce in the (Ce,Fe)-rich region also confirms Ce $\text{FeO}_3$  formation.

In line with the electron microscopy observations it is suggested that the layers on the Fe–Cr alloy is firstly, a (Cr,Mn)-oxide spinel, followed by a Cr-oxide, and a predominately Ce $\text{FeO}_3$  layer. The ScYSZ surface is coated with both a CGO and a Ce $\text{FeO}_3$  layer (Fig. 11).

#### 4. Discussion

##### 4.1. Oxide scale formation and effect of CGO infiltration

From the half cell corrosion study it is clear that CGO infiltration improves the Fe–Cr alloy oxidation resistance. Several studies have investigated the benefits of adding so-called reactive elements (e.g. in the form of  $\text{CeO}_2$ ) on the ferrous Fe–Cr alloy systems – known as the reactive element effect (REE). The REE is typically attributed to improve scale-alloy adhesion avoiding scale spallation and to a lowering of the oxidation rate [13]. The present study shows that the

uninfiltrated samples exhibit extensive breakaway oxidation leaving the metallic particles completely oxidized, while a thin adherent oxide scale is formed on the infiltrated samples, suggesting REE.

In the present study a small amount of (Cr,Mn)-oxide spinel, followed by chromia, and a Ce $\text{FeO}_3$  layer is observed. Previous oxidation studies of ferritic Fe–Cr alloys, containing small Mn concentrations, have observed an oxide scale consisting of chromium oxide and a manganese chromium spinel [14–16]. Typically, with a  $\text{Cr}_2\text{O}_3$  inner layer and an  $(\text{Mn},\text{Cr})_3\text{O}_4$  outer layer, but Mn-rich zones have also previously been identified at the alloy–chromia interface (see e.g. [17]).

The Ce $\text{FeO}_3$  layer observed in this study is suggested to be formed during the initial transient oxidation phase, where a dense continuous chromia scale is not yet formed. During this transient phase, both manganese and chromium will oxidize, while iron will diffuse outwards and react with  $\text{CeO}_2$  to form Ce $\text{FeO}_3$ . There are a few reports in the literature confirming the formation of Ce $\text{FeO}_3$  upon addition of cerium to the surfaces of various steels and pure iron [18]. It has been suggested that the presence of  $\text{Ce}^{3+}$ , found in the Ce $\text{FeO}_3$ , has a beneficial effect on improving the high temperature oxidation resistance of stainless steel [19]. After a period, a thin continuous layer of chromia will form. This will define a  $p\text{O}_2$  of  $2.2 \times 10^{-27}$  Pa at the alloy–chromia interface, which will prevent iron from oxidation and diffusion through the dense chromia layer (determined from Ellingham diagram).

##### 4.2. Metal supported cell durability

During MSC durability testing the MSC degradation is characterised by a linear increase in the  $R_s$  (concomitant with anode in-plane resistivity increase) and a minor  $R_p$  increase. The increased  $R_p$  is characterised by an increase at high ( $>10$  kHz) and intermediate (500 Hz) frequencies which have previously been ascribed to the formation of one, or more, insulating layers and an increased fuel oxidation resistance, respectively [9].

From microstructural investigation it is observed that during durability testing an oxide layer of ca. 500 nm forms on the Fe–Cr

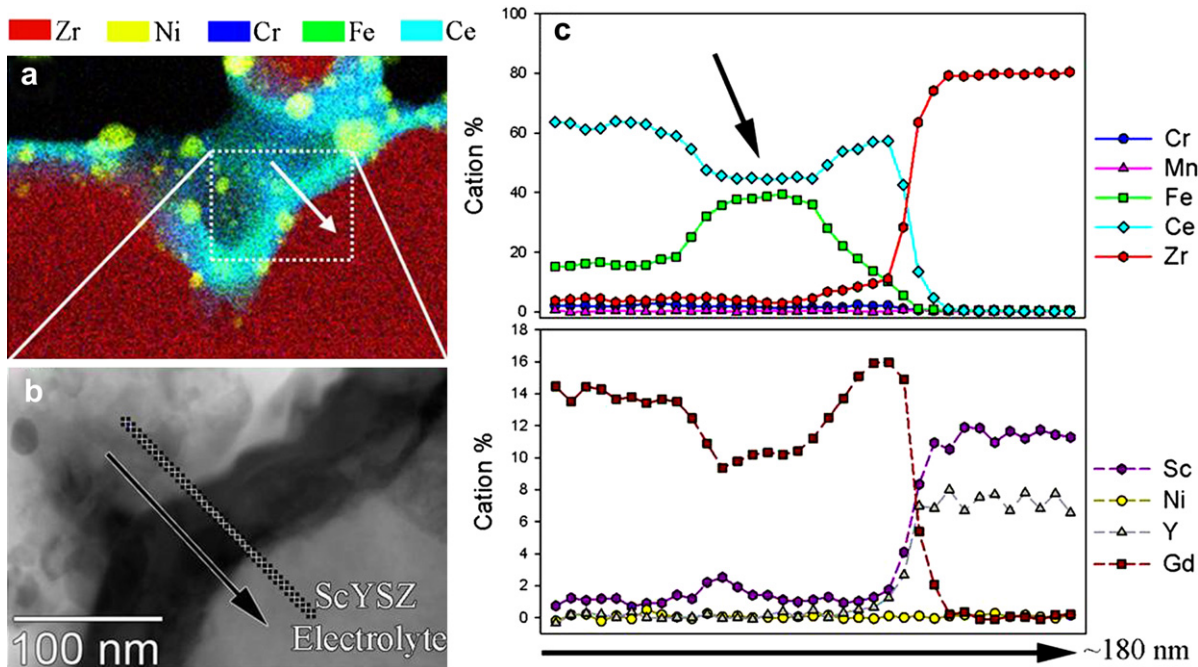


**Fig. 7.** (a) STEM-EDS of CGO-Ni on YSZ in tested MSC – superimposed Zr, Ni, Cr, Fe and Ce elemental maps, (b) the BF-STEM micrograph of the box in (a) illustrating the position of line scan EDS, and (c) the resulting concentration profile.

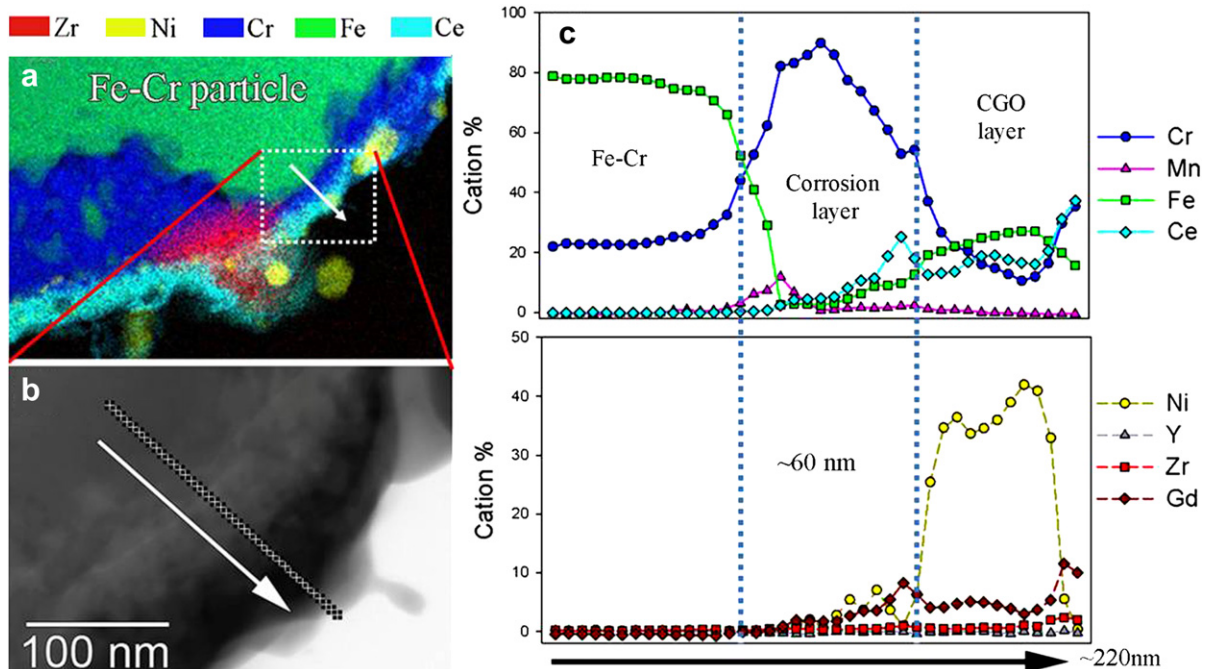


**Fig. 8.** (a) STEM-EDS of CGO-Ni on Fe–Cr alloy in tested MSC – superimposed Zr, Ni, Cr, Fe and Ce elemental maps, (b) BF-STEM micrograph of the box in (a) illustrating the position of line scan EDS, and (c) the resulting concentration profile.

alloy near the TPBs sites, which is considerably thicker than the 40 nm forming around the rest of the alloy (Fig. 4) or the 90 nm thick oxide layer in the reference cell (Fig. 3(b)). This accelerated oxidation process at the TPBs may be clarified by considering the MSC anode TPBs.

For electrochemical oxidation of a fuel, e.g. hydrogen (Equation (1)), an oxidation catalyst and a TPB is required. In the current study, Ni is used as the main catalyst for the dissociative adsorption of hydrogen, but  $\text{CeO}_2$  and doped  $\text{CeO}_2$  (e.g. CGO) are also

promising hydrogen electro-oxidation materials in SOFCs [20–24] and  $\text{CeFeO}_3$  has also been reported to have some capability of partial oxidation of methane to CO and  $\text{H}_2$  [25].



A TPB is a physical site where the gas phase meets the electronic and ionic conducting phase. For electronic/ionic transport to and from the TPB the main electronic path is through the Fe–Cr to the current collect and the  $\text{O}^{2-}$  conduction path is from the cathode and through the YSZ/ScYSZ (Fig. 11(a)). The infiltrated CGO and the new reaction layers will alter the electronic/ionic pathways. CGO is both an electronic and oxide ion conductor at the temperatures and

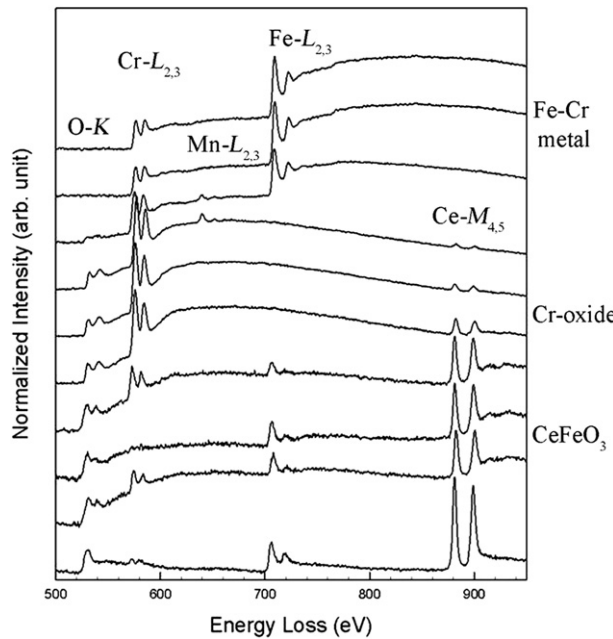


**Fig. 9.** STEM-EELS across Fe–Cr alloy (top), oxide scale (middle),  $\text{CeFeO}_3$  interface (bottom) in Fig. 8(b). The spectra are collected at a spacing of ca. 13 nm, starting in the Fe–Cr alloy (top) and terminating in the  $\text{CeFeO}_3$  (bottom).

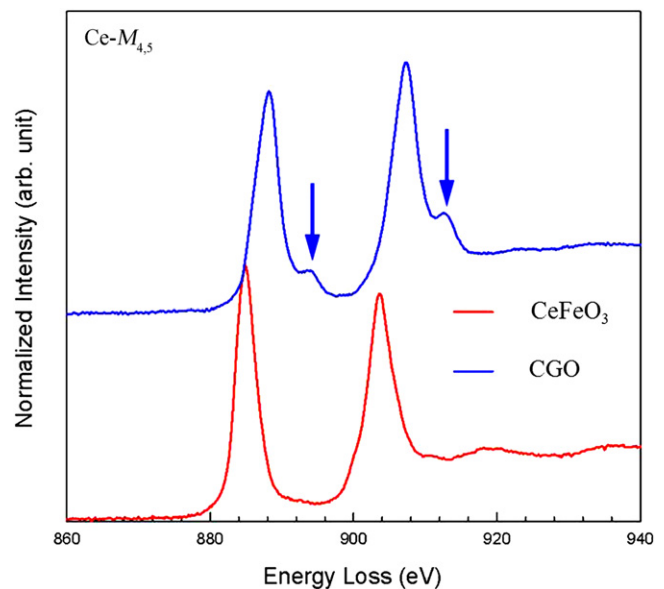


**Fig. 10.** EELS of  $\text{Ce}^{4+}$  in CGO vs.  $\text{Ce}^{3+}$  found in  $\text{CeFeO}_3$  in tested MSC.

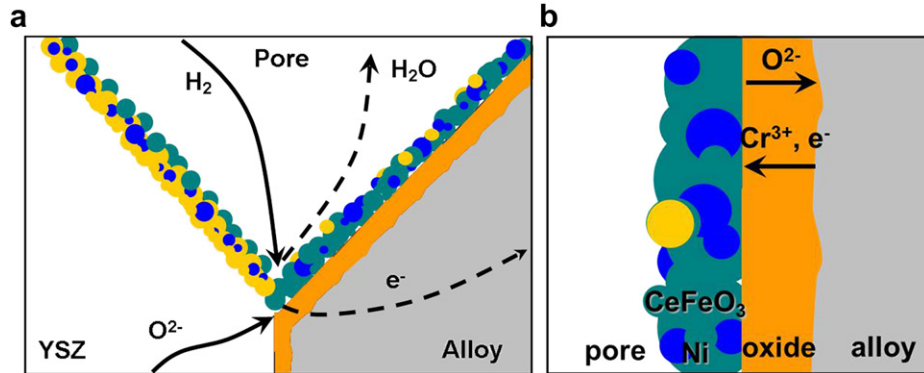


**Fig. 11.** (a) Schematic of TPB illustrating the  $O^{2-}$  and  $H_2$  transport to the TPB and the  $H_2O$  and electron transport away from the TPB. (b) Schematic of the  $O^{2-}$ ,  $Cr^{3+}$  and  $e^-$  transport through the  $Cr_2O_3$  layer under OCV conditions [30]. Yellow – CGO, Blue – Ni, Green – CeFeO<sub>3</sub>, Orange –  $Cr_2O_3$ . (For interpretation of the references to colour in this figure legend, the reader is referred to the web version of this article.)

low  $pO_2$  conditions investigated [26]. However, in the MSC anode, the CGO adjacent to the alloy and YSZ is partially converted to CeFeO<sub>3</sub>. Although there are no reports on the ionic or electronic conductivity of CeFeO<sub>3</sub>, the strongly orthorhombic structure of CeFeO<sub>3</sub> is not considered favourable for ionic conductivity [27]. Chromia, which forms on the alloy surface exhibits poor electronic conductivity [28] so new TPBs will not be created as the result of chromia formation. As such, the major TPB regions are considered the Ni-CGO and the CGO in the alloy-YSZ intersection points (Fig. 11(a)).

At 650 °C, with 3%  $H_2O/H_2$  supplied to the anode, the  $pO_2$  is ca.  $4.6 \times 10^{-21}$  Pa ( $4.5 \times 10^{-26}$  atm) (Appendix A). Under these conditions, the oxide scale on the Fe–Cr alloy will continue to form. However, at the active TPB sites, a higher  $pO_2$  will equilibrate which can be estimated from the Nernst equation. With a cell overvoltage of 330 mV, of which approximately 30% is attributed to anode losses, a  $pO_2$  of  $8.1 \times 10^{-18}$  Pa ( $8.0 \times 10^{-23}$  atm) will equilibrate at the TPB (Appendix A). In comparison the reference test (Fig. 3(b)), which was tested in more oxidising conditions ( $pH_2O/pH_2 = 9$ ;  $pO_2 = 4.11 \times 10^{-16}$  Pa or  $4.05 \times 10^{-21}$  atm) for a longer duration (2000 h vs. 170 h), shows less oxidation than the TPBs in the tested cell. Therefore, an increased  $pO_2$  at the TPB cannot simply explain the observed accelerated oxidation. Rather, it is proposed that the imposed electric field accelerates oxidation.

At OCV, during alloy oxidation,  $Cr^{3+}$  diffuses outwards and  $O^{2-}$  diffuses inwards, which is accompanied by an outward transport of electrons (Fig. 11(b)) [29]. Thus, when an external electric field is applied (i.e. during MSC operation) the driving force for ions may be increased or decreased (depending on field bias). In this case, the fuel is oxidized and electrons are transported through the oxide scale into the alloy matrix. This will increase the driving force for the outward diffusion of metal cations and inward diffusion of oxide ions, and thus increase the oxidation rate [30].

The rate at which this oxidation will be accelerated can be understood considering Equation (2) [29].

$$\frac{dx}{dt} = \frac{k_p}{x} + \frac{I_{ext}t_{ion}}{6e} \cdot \frac{M(Cr_2O_3)}{\rho(Cr_2O_3)N_A} \quad (2)$$

The first term in this equation is the normal parabolic oxidation, while the second term is the effect of applying the external current  $I_{ext}$ .  $t_{ion}$  is the ionic transference number,  $e$  the elementary charge,  $M(Cr_2O_3)$  the molecular weight,  $\rho$  the density, and  $N_A$  Avogadro's number. Thus the oxidation rate will be increased or decreased depending on the sign of  $I_{ext}$ . The effect of the current is relatively small given the low ionic transference number for chromia and the

relatively small current density applied ( $0.25 \text{ A cm}^{-2}$ ). However, given the cermet microstructure the local current density would be higher. As such, it is postulated that the favourable bias in conjunction with the locally high current density causes increased oxidation rate at the TPB, yielding an increase  $R_s$  and  $R_p$  during fuel cell operation.

## 5. Conclusions

Infiltration of Ni-CGO into the Fe–Cr alloy/YSZ anode cermet of a metal supported SOFC, coats the Fe–Cr particles and YSZ particles evenly. From TEM-EDS and EELS analysis it is concluded that irrespective of whether the CGO is located on the YSZ or the Fe–Cr particles, the CGO can be converted to CeFeO<sub>3</sub> – however more CGO is converted to CeFeO<sub>3</sub> on the Fe–Cr particles.

Electron microscopy investigation of oxidised, infiltrated or uninfiltrated cermets shows that the significantly improved oxidation resistance is provided to the Fe–Cr alloy through the CGO infiltration.

Fuel cell testing of an infiltrated metal supported cell, shows generally excellent oxidation resistance, however, at the TPBs accelerated oxidation is observed. During fuel cell testing a bias needs to establish across the oxide layer in the TPB region, to draw electrons from the TPB, across the oxidation layer, to the Fe–Cr alloy. The accelerated oxidation at the TPBs, during fuel cell testing, is attributed to this imposed bias established during SOFC testing.

## Acknowledgements

Financial support by Topsoe Fuel Cell, the EU project FP7-211940 (METSOFC), and The Danish National Advanced Technology Foundation is gratefully acknowledged. Per Hjalmarsson is also acknowledged for his assistance in EIS modelling.

## Appendix A

The oxygen partial pressure in a steam/hydrogen environment can be determined by Equation (3) [31], which is valid for 1000–1300 K:

$$pO_2 = \left( k_p \frac{pH_2O}{pH_2} \right)^2 = \left( 10^{2.958 - 13022/T} pH_2O \right)^2 \quad (3)$$

where,  $p$  is in atm and  $T$  is in K.

Once the oxygen partial pressure is known in the electrode, the oxygen partial pressure at the electrode/electrolyte interface can be calculated, if the electrode overvoltage is known using the Nernst equation:

$$p_{O_2, \text{interface}} = \frac{p_{O_2}}{\exp \frac{4\eta F}{RT}} \quad (4)$$

where,  $\eta$  is the electrode overpotential (V),  $p_{O_2}$  is the oxygen partial pressure supplied to the electrode,  $p_{O_2, \text{interface}}$  is the equilibrium  $p_{O_2}$  at the electrode/electrolyte interface and  $F$  and  $R$  have the usual meaning.

## References

- [1] S. Haile, *Acta Mater.* 51 (2003) 5981–6000.
- [2] A.J. Jacobson, *Chem. Mater.* 22 (2010) 660–674.
- [3] N.Q. Minh, *J. Am. Ceram. Soc.* 76 (1993) 563–588.
- [4] S.C. Singhal, K. Kendall, *High Temperature Solid Oxide Fuel Cells: Fundamentals, Design and Applications*, Elsevier Advanced Tech., Oxford, 2003.
- [5] M.C. Tucker, G.Y. Lau, C.P. Jacobson, L.C. DeJonghe, S.J. Visco, *J. Power Sources* 171 (2007) 477–482.
- [6] M.C. Tucker, *J. Power Sources* 195 (2010) 4570–4582.
- [7] M. Brandner, M. Bram, J. Froitzheim, H.P. Buchkremer, D. Stoever, *Solid State Ionics* 179 (2008) 1501–1504.
- [8] P. Blennow, J. Hjelm, T. Klemensø, Å.H. Persson, S. Ramousse, M. Mogensen, *Fuel Cells* 11 (2011) 661–668.
- [9] P. Blennow, J. Hjelm, T. Klemensø, S. Ramousse, A. Kromp, A. Leonide, A. Weber, *J. Power Sources* 196 (2011) 7117–7125.
- [10] R. Knibbe, A. Hauch, J. Hjelm, S.D. Ebbesen, M. Mogensen, *Green* 1 (2011) 141–169.
- [11] P. Blennow, M. Mogensen, Patent EP2031675 (2011).
- [12] L.A.J. Garvie, P.R. Buseck, *J. Phys. Chem. Solids* 60 (1999) 1943–1947.
- [13] B.A. Pint, *Oxid. Met.* 45 (1996) 1–37.
- [14] J. Froitzheim, G.H. Meier, L. Niewolak, P.J. Ennis, H. Hattendorf, L. Singheiser, W.J. Quadakkers, *J. Power Sources* 178 (2008) 163–173.
- [15] J. Froitzheim, H. Ravash, E. Larsson, L.G. Johansson, J.E. Svensson, *J. Electrochem. Soc.* 157 (2010) B1295–B1300.
- [16] W.J. Quadakkers, J. Piron-Abellan, V. Shemet, L. Singheiser, *Mater. High Temp* 20 (2003) 115–127.
- [17] P. Huczkowski, N. Christiansen, V. Shemet, L. Niewolak, J. Piron-Abellan, L. Singheiser, W.J. Quadakkers, *Fuel Cells* 6 (2006) 93–99.
- [18] H. Buscail, J.P. Larpin, *Solid State Ionics* 92 (1996) 243–251.
- [19] S. Patil, S.C. Kuiry, S. Seal, *Proc. R. Soc. London Ser. A* 460 (2004) 3569–3587.
- [20] R.J. Gorte, J.M. Vohs, *Annu. Rev. Chem. Biomol. Eng.* 2 (2011) 9–30.
- [21] O.A. Marina, C. Bagger, S. Primdahl, M. Mogensen, *Solid State Ionics* 123 (1999) 199–208.
- [22] S. Primdahl, M. Mogensen, *Solid State Ionics* 152–153 (2002) 597–608.
- [23] E.S. Putna, J. Stubenrauch, J.M. Vohs, R.J. Gorte, *Langmuir* 11 (12) (1995) 4832–4837.
- [24] B.C.H. Steele, P.H. Middleton, R.A. Rudkin, *Solid State Ionics* 40–41 (1990) 388–393.
- [25] K. Li, H. Wang, Y. Wei, M. Liu, *J. Rare Earths* 26 (2008) 705–710.
- [26] M. Mogensen, N.M. Sammes, G.A. Tompsett, *Solid State Ionics* 129 (2000) 63–94.
- [27] M. Mogensen, D. Lybye, N. Bonanos, P.V. Hendriksen, F.W. Poulsen, *Solid State Ionics* 174 (2004) 279–286.
- [28] A. Holt, P. Kofstad, *Solid State Ionics* 69 (1994) 137–143.
- [29] P. Kofstad, *High Temperature Corrosion*, Elsevier Applied Science Pub., Essex, 1988, pp. 163–205.
- [30] Y. Li, Y. Jiang, J. Wu, R. Pineault, R. Gemmenn, X. Liu, *Int. J. Appl. Ceram. Technol.* 7 (2010) 41–48.
- [31] R. Hartung, H.H. Möbius, *Chem. Ing. Tech.* 40 (1968) 592–600.